The Antarctic Atmospheric Energy Budget. Part II: The Effect of Ozone Depletion and its Projected Recovery

KAREN L. SMITH AND MICHAEL PREVIDI

Lamont-Doherty Earth Observatory, Palisades, New York

LORENZO M. POLVANI

Department of Applied Physics and Mathematics, Department of Earth and Environmental Sciences, Columbia University, New York, New York

(Manuscript received 13 March 2013, in final form 12 June 2013)

ABSTRACT

In this study the authors continue their investigation of the atmospheric energy budget of the Antarctic polar cap (the region poleward of 70°S) using integrations of the Whole Atmosphere Community Climate Model from the years 1960 to 2065. In agreement with observational data, it is found that the climatological mean net top-of-atmosphere (TOA) radiative flux is primarily balanced by the horizontal energy flux convergence over the polar cap. On interannual time scales, changes in the net TOA radiative flux are also primarily balanced by changes in the energy flux convergence, with the variability in both terms significantly correlated (positively and negatively, respectively) with the southern annular mode (SAM). On multidecadal time scales, twentieth-century stratospheric ozone depletion produces a negative trend in the net TOA radiative flux due to a decrease in the absorbed solar radiation within the atmosphere–surface column. The negative trend in the net TOA radiative flux is balanced by a positive trend in energy flux convergence, primarily in austral summer. This negative (positive) trend in the net TOA radiation (energy flux convergence) occurs despite a positive trend in the SAM, suggesting that the effects of the SAM on the energy budget are overwhelmed by the direct radiative effects of ozone depletion. In the twenty-first century, ozone recovery is expected to reverse the negative trend in the net TOA radiative flux, which would then, again, be balanced by a decrease in the energy flux convergence. Therefore, over the next several decades, ozone recovery will, in all likelihood, mask the effect of greenhouse gas warming on the Antarctic energy budget.

1. Introduction

The dominant driver of recent multidecadal change in the Antarctic climate system has been the depletion of stratospheric ozone [see Thompson et al. (2011) for a recent review]. The formation of the ozone hole over the South Pole has been associated with a cooling of the stratosphere and much of the Antarctic continent, a warming of the Antarctic peninsula (Steig et al. 2009), a poleward shift of the storm tracks (Polvani et al. 2011b; Son et al. 2010, 2009; Lee and Feldstein 2013), a poleward shift in subtropical precipitation (Kang et al. 2011), and changes in Southern Ocean mixing and ventilation (Sallée et al. 2010; Waugh et al. 2013). The changes in the atmospheric circulation (i.e., lowered geopotential heights over Antarctica and raised geopotential heights over the southern midlatitudes, resulting in strengthened westerlies) are characteristic of the southern annular mode (SAM), the dominant mode of Southern Hemisphere extratropical circulation variability, which has been experiencing a positive trend over the past several decades. Despite the many studies examining the role of ozone depletion in large-scale atmospheric circulation trends, none has examined the implications of ozone depletion for atmospheric energy transport into the Antarctic polar cap.

Compared to the Arctic, the atmospheric energy budget of the Antarctic has received relatively little attention (Cullather and Bosilovich 2012; Genthon and Krinner 1998; Nakamura and Oort 1988). Arctic climate change, including dramatic sea ice loss and surface and

Corresponding author address: Karen L. Smith, Lamont-Doherty Earth Observatory, 207B Oceanography, 61 Route 9W, P.O. Box 1000, Palisades, NY 10964.
E-mail: ksmith@ldeo.columbia.edu

DOI: 10.1175/JCLI-D-13-00173.1

midtropospheric warming, has motivated numerous studies of the energy budget in this region (Kay et al. 2012; Cullather and Bosilovich 2012; Porter et al. 2010; Serreze et al. 2007; Nakamura and Oort 1988). Although the Antarctic has not experienced comparable polar amplification, the dramatic change in the top-of-atmosphere (TOA) shortwave radiative flux associated with Southern Hemisphere stratospheric ozone depletion has likely had an important influence on the Antarctic energy budget. In addition, the recovery of stratospheric ozone in the future may influence the degree of Southern Hemisphere polar amplification we can expect in the coming decades.

In Part I, Previdi et al. (2013, hereafter Part I), we examined the climatological mean and intraseasonal-to-interannual variability of the components of the Antarctic energy budget using reanalysis and satellite data, and found a two-way balance between the net TOA radiative flux and the horizontal energy flux convergence over the polar cap. This two-way balance is reflected in significant and opposite-signed correlations between these terms and the SAM; the net TOA radiative flux is positively correlated with the SAM while the energy flux convergence is negatively correlated with the SAM. In light of the positive trend in the SAM over the past few decades, can one infer from interannual relationships that net TOA flux has been increasing and the energy flux convergence has been decreasing over this time period? This question will be addressed in this study.

Although direct observation of the Antarctic climate system over the past several decades has improved, observation of the climate of the high southern latitudes continues to be spatially and temporally limited; thus, we need to rely on models and reanalyses to aid us in estimating and interpreting the changes that have occurred. The lack of continuous observational data is a particular hindrance for assessing the multidecadal effect of ozone depletion on the Antarctic energy budget. First, there is no record of the TOA radiative fluxes prior to the formation of the ozone hole. Second, direct satellite measurements of the TOA radiative fluxes in the period since consist of short and discontinuous time series. The longest and most recent record is the Clouds and the Earth's Radiant Energy System (CERES) dataset that began in March 2000. However, during the period from 2000 to the present, ozone levels in the Southern Hemisphere have leveled off due to global regulations on chlorofluorocarbons (CFCs; Scientific Assessment of Ozone Depletion; WMO 2010), making this time period inappropriate for detecting TOA trends due to ozone depletion.

The other satellite time series of TOA fluxes is from the Earth Radiation Budget Experiment (ERBE), which ran from February 1985 to April 1989. This is a short dataset and it is difficult to directly compare it with CERES, given that they are derived from different instruments with their own biases. After some bias correction, Fasullo and Trenberth (2008) show significant differences between climatological ERBE and CERES net TOA shortwave and longwave radiative fluxes at high southern latitudes in austral spring, consistent with the effect of ozone depletion (a decrease in both absorbed solar and outgoing longwave radiation in CERES relative to ERBE; see their Fig. 1). It is difficult to attribute these differences to ozone, however, given that differences between the two datasets are significant in many other parts of the globe and at other times of the year (i.e., when ozone depletion would be expected to be unimportant). Furthermore, the CERES dataset includes the September 2002 stratospheric sudden warming, which has likely skewed the springtime mean of the net TOA flux in CERES over Antarctica given that sudden warmings in the Southern Hemisphere are very rare (the September 2002 TOA longwave flux anomaly averaged from 70° to 90°S was more than two standard deviations outside the 2001–10 CERES mean).

Reanalyses are extremely useful tools for investigating the climate of the recent past; however, because of the adverse effect of biases in observed ozone on the analysis, reanalysis products do not assimilate time-varying ozone data using analysis schemes that allow ozone to interact with other dynamical fields (Dee et al. 2011). In addition, reanalyses of the high-latitude Southern Hemisphere prior to the satellite era are poorly constrained by observations and must be used with caution (Kistler et al. 2001).

To circumvent the issues with satellite and reanalysis data, we investigate the extent to which ozone depletion and projected recovery influence the Antarctic energy budget using a fully coupled, state-of-the-art, stratosphere-resolving model with interactive stratospheric chemistry. In addition to investigating the trends in the Antarctic energy budget in an ensemble of twentieth-century model integrations, we also compare two ensembles of twenty-first-century integrations, one with and one without ozone recovery. We find that trends in the Antarctic energy budget in the twentieth century are dominated by the effects of ozone depletion, particularly the TOA shortwave radiative flux in spring and summer. In the future, ozone recovery should reverse these trends.

2. Methods

a. Model

We employ the Community Earth System Model version 1 (CESM1) using the Whole Atmosphere Community Climate Model atmospheric component [CESM1 (WACCM); hereafter simply WACCM], that is, the

stratosphere-resolving, coupled-chemistry version of the National Center for Atmospheric Research (NCAR) Community Atmosphere Model version 4 (CAM4) (Gent et al. 2011). The land, ocean, and sea ice components of WACCM are identical to those in CESM1. In contrast, the WACCM atmospheric component has 66 vertical levels with a model top at 140 km, a horizontal resolution of 1.9° × 2.5°, special parameterizations for gravity waves and other upper atmospheric processes, and, most importantly, fully interactive stratospheric chemistry.

The WACCM twentieth-century ensemble comprises three integrations and extends from 1960 to 2000 (labeled 20C). These integrations follow the Coupled Model Intercomparison Project phase 5 (CMIP5) Historical scenario for surface greenhouse gas concentrations (Meinshausen et al. 2011). The Historical scenario also includes prescribed surface concentrations of ozone-depleting substances (ODSs). For further details on the model and the twentieth-century integrations the reader is referred to Marsh et al. (2013).

To examine the role of ozone recovery in the twenty-first century we contrast two ensembles of model runs, each comprising three integrations, from 2001 to 2065. These model integrations were previously examined in Smith et al. (2012) for Antarctic sea ice. For the first ensemble (labeled 21C), forcings for the years 2001–05 are specified following the CMIP5 Historical scenario and forcings for the years 2006–65 are specified following representative concentration pathway 4.5 (RCP 4.5; Meinshausen et al. 2011). The RCP 4.5 members are initialized from the three corresponding Historical integrations described above (Marsh et al. 2013). For the second twenty-first century ensemble (labeled FixODS), everything is identical to 21C except for the surface concentrations of ODSs, which are held fixed at year 2000 levels. In other words, we compare two future scenarios in which greenhouse gas (GHG) concentrations increase, but one includes ozone recovery (21C) and the other does not (FixODS). This is shown in Fig. 1a, where we plot the ensemble mean October–December (OND) total column ozone, averaged over 70°–90°S, for the twentieth-century ensemble and for both twenty-first-century ensembles. Southern Hemisphere polar cap ozone decreases dramatically from 1965 to 2000 (black curve). From 2001 onward, ozone recovers for the 21C scenario (black curve) but remains constant for the FixODS scenario (red curve).

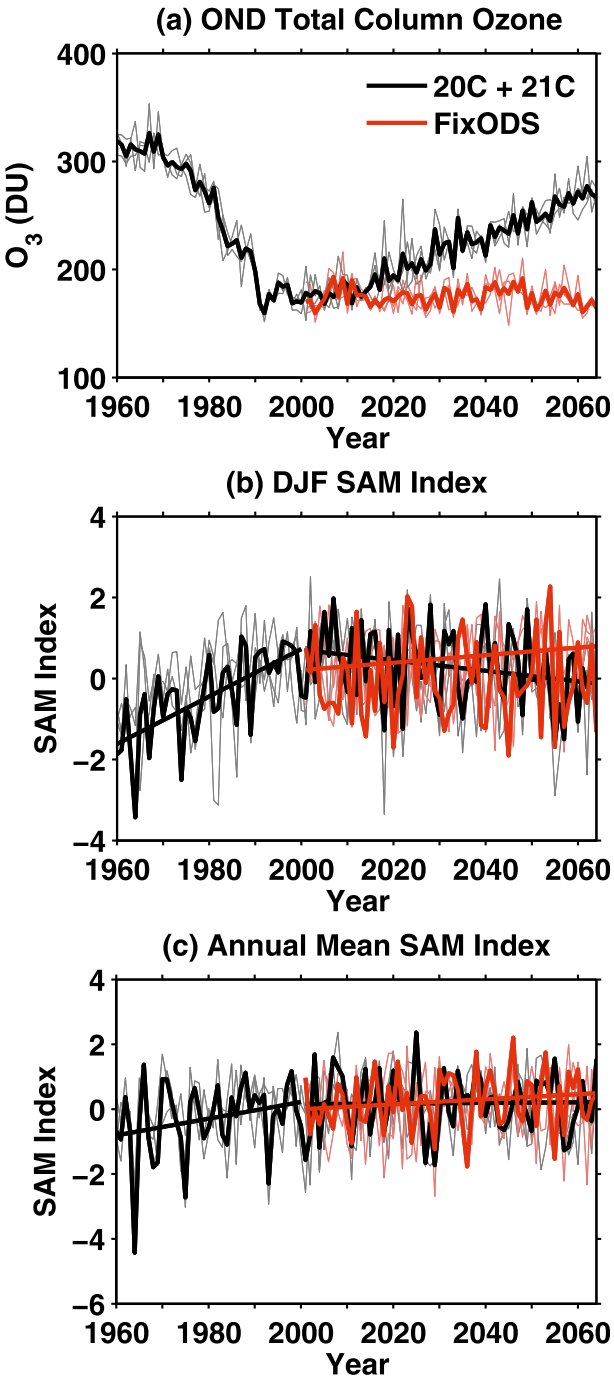

FIG. 1. WACCM time series of (a) polar cap averaged (70°–90°S) October–December (OND) total column ozone, (b) December–February (DJF) SAM, and (c) annual mean SAM for the years 1960–2065. Black curve indicates the 20C and 21C scenarios and red curve indicates the FixODS scenario (ensemble means). Individual ensemble members are shown in thin gray and pink curves.

b. *Energy budget*

We define the energy budget of the atmosphere as

$$\frac{\partial E}{\partial t} = F_{\mathrm{TOA:NET}} + F_{\mathrm{SFC:NET}} + F_{\mathrm{WALL}}, \qquad (1)$$

where $\partial E/\partial t$ is the vertically integrated atmospheric energy storage, $F_{\mathrm{TOA:NET}}$ is the net top-of-atmosphere (TOA) radiative flux, $F_{\mathrm{SFC:NET}}$ is the net surface energy flux (including radiative, sensible, and latent heat fluxes), and F_{WALL} is the vertically integrated horizontal energy flux convergence. The energy storage term can be written as

$$\frac{\partial E}{\partial t} = \frac{\partial}{\partial t}\int_0^{p_s} (c_p T + \Phi_s + Lq + k)\frac{dp}{g}, \tag{2}$$

where g is the gravitational acceleration, p is pressure, p_s is the surface pressure, c_p is the specific heat of air at constant pressure, T is the absolute temperature, Φ_s is the surface geopotential, L is the latent heat of vaporization for water, q is the specific humidity, and k is the kinetic energy. The dry static energy (DSE) is the sum of the internal energy, c_pT, and the potential energy, Φ, and the moist static energy (MSE) is the DSE plus the latent energy, Lq. The terms on the right-hand side of Eq. (1) consist of the following components:

$$F_{\mathrm{TOA:NET}} = F_{\mathrm{TOA:SW}} + F_{\mathrm{TOA:LW}}, \tag{3}$$

$$F_{\mathrm{SFC:NET}} = F_{\mathrm{SFC:SW}} + F_{\mathrm{SFC:LW}} + F_{\mathrm{SFC:LH+SH}}, \tag{4}$$

$$F_{\mathrm{WALL}} = -\nabla \cdot \int_0^{p_s} (c_p T + \Phi + Lq + k)\mathbf{v}\frac{dp}{g}. \tag{5}$$

Note that $F_{\mathrm{TOA:NET}}$ [Eq. (3)] consists of the net TOA shortwave (SW) and longwave (LW) radiative fluxes, $F_{\mathrm{TOA:SW}}$ and $F_{\mathrm{TOA:LW}}$, respectively. These fluxes are alternatively known as the absorbed solar radiation (ASR) and outgoing longwave radiation (OLR). Equation (4) states that $F_{\mathrm{SFC:NET}}$ consists of the net surface SW and LW radiative fluxes, $F_{\mathrm{SFC:SW}}$ and $F_{\mathrm{SFC:LW}}$, and the net turbulent flux of sensible heat (SH) plus latent heat (LH), $F_{\mathrm{SFC:LH+SH}}$. The default $F_{\mathrm{SFC:LH}}$ output by WACCM does not account for the latent heat of snowmelt. This has been included by calculating the latent heat flux associated with snowfall following the method of Kay et al. (2012). Finally, Eq. (5) states that F_{WALL} consists of the convergence of the vertically integrated horizontal flux of MSE plus kinetic energy k, where υ is the horizontal wind vector. A complete derivation of Eqs. (1)–(5) is given in appendix A.

TOA and surface fluxes (in $\mathrm{W\,m^{-2}}$) are obtained from monthly model output, and $\partial E/\partial t$ was calculated using daily model output following the method of Trenberth (1991). The term F_{WALL} is calculated as a residual of the other budget terms (Kay et al. 2012; Porter et al. 2010). All other model output used in this study, such as sea level pressure (SLP), surface air temperature (SAT), and cloud properties, is obtained from monthly model output. The Antarctic energy budget terms are defined as area-weighted averages over the polar cap (70°–90°S). By convention, positive energy budget terms indicate that the atmospheric column is gaining energy while negative terms indicate that the atmospheric column is losing energy.

Following Part I, we focus on how the energy budget is affected by variability in the SAM. The SAM index is computed using the monthly or seasonal zonal mean difference between standardized SLP anomalies at 40° and 65°S (Marshall 2003).

Finally, in section 3b, when calculating correlations between the Antarctic energy budget components and the SAM, the full 1960–2065 anomaly time series of the data are detrended piecewise and linearly due to visible changes in magnitudes and/or signs of the trends in the Antarctic resulting from the transition between stratospheric ozone depletion (20C) and future recovery (21C). To do this, we specify two adjacent segments of time series [1960–2000 (20C) and 2001–65 (21C)] with a shared data point at the year 2000 and remove a continuous, piecewise linear trend from the full 1960–2065 time series. We have conducted the same analysis for the 20C plus FixODS time series and find that the results are very similar.

3. Results

a. Climatological energy budget

In the following two sections, we validate the suitability of using WACCM to investigate trends in the Antarctic energy budget. In this section, we first establish how well WACCM simulates the climatological mean Antarctic energy budget. We compare the model budget for the years 2001–10 with the observational estimate of Part I. Overall, WACCM simulates the climatological Antarctic energy budget quite well.

Table 1 lists the 2001–10 climatological mean Antarctic energy budget based on the ensemble mean of the WACCM twenty-first century (21C) integrations. The key feature of Table 1 is that the dominant energy balance is between net TOA radiative flux and the horizontal energy flux convergence, $F_{\mathrm{TOA:NET}}$ and F_{WALL} (except in December). The net surface flux ($F_{\mathrm{SFC:NET}}$) and the energy storage ($\partial E/\partial t$) are generally small. The values for $F_{\mathrm{SFC:NET}}$, $\partial E/\partial t$, $F_{\mathrm{TOA:NET}}$, and F_{WALL} from Table 1 are also shown in the solid lines in Fig. 2. The climatology shown in Fig. 2 agrees well with the observational estimates of Part I (dashed lines in Fig. 2).

The net TOA radiative flux ($F_{\mathrm{TOA:NET}}$) is negative throughout the year, indicating a net flux of energy from the atmospheric column to space. In winter, the net TOA SW flux, $F_{\mathrm{TOA:SW}}$, is essentially zero over the Antarctic polar cap and the net TOA LW flux, $F_{\mathrm{TOA:LW}}$, is balanced

TABLE 1. Monthly and annual mean WACCM climatological mean Antarctic energy budget components for 2001–10. Values are based on the ensemble mean of the WACCM twenty-first century (21C) integrations. All values are in W m^{-2} with positive values indicating energy gain by the atmospheric column.

	$\frac{\partial E}{\partial t}$	$F_{\mathrm{TOA:SW}}$	$F_{\mathrm{TOA:LW}}$	$F_{\mathrm{TOA:NET}}$	$F_{\mathrm{SFC:SW}}$	$F_{\mathrm{SFC:LW}}$	$F_{\mathrm{SFC:LH+SH}}$	$F_{\mathrm{SFC:NET}}$	F_{WALL}
Jan	7	164	−194	−30	−81	59	6	−16	51
Feb	−8	106	−182	−76	−50	51	−1	0	66
Mar	−19	41	−163	−122	−17	42	−11	14	87
Apr	−15	7	−148	−141	−2	36	−21	13	110
May	−13	1	−140	−139	0	35	−23	12	113
Jun	−7	0	−131	−131	0	35	−23	12	110
Jul	−6	0	−125	−125	0	35	−23	12	104
Aug	−1	2	−125	−123	−1	36	−23	12	107
Sep	6	18	−131	−113	−7	38	−21	10	106
Oct	12	60	−144	−84	−27	45	−13	5	89
Nov	20	121	−165	−44	−58	55	−3	−6	68
Dec	23	168	−186	−18	−83	61	5	−17	56
Annual	0	57	−153	−95	−27	44	−13	4	89

by F_{WALL}, whereas in summer $F_{\mathrm{TOA:SW}}$ and $F_{\mathrm{TOA:LW}}$ offset each other significantly, resulting in weaker horizontal energy transport. Consequently, $F_{\mathrm{TOA:NET}}$ and F_{WALL} have pronounced seasonal cycles.

Although the net surface flux ($F_{\mathrm{SFC:NET}}$) tends to be small, it reflects the cancellation of larger-magnitude radiative and turbulent flux components. The net surface SW flux ($F_{\mathrm{SFC:SW}}$) follows the seasonal cycle of TOA insolation. The net surface LW flux ($F_{\mathrm{SFC:LW}}$) varies seasonally in a manner similar to $F_{\mathrm{TOA:LW}}$; when surface temperatures are highest in austral summer, $F_{\mathrm{SFC:LW}}$ is at a maximum. The turbulent fluxes of moisture and heat ($F_{\mathrm{SFC:LH+SH}}$) are negative throughout most of the year except in December and January. Similar to what we reported in Part I, we find that the seasonal cycle of $F_{\mathrm{SFC:LH+SH}}$ in WACCM is driven by the sensible heat fluxes. The wintertime near-surface temperature inversion over the Antarctic (Fig. 3, solid curve) leads to sensible heat fluxes from the atmosphere to the surface. From winter to summer, as surface temperatures increase and the inversion weakens (Fig. 3, dashed curve), sensible heat fluxes decrease and latent heat fluxes from the surface to the atmosphere increase slightly resulting in positive $F_{\mathrm{SFC:LH+SH}}$ fluxes in December and January.

As pointed out in Part I, the different characteristics (e.g., heat capacity, albedo) of the underlying surfaces in the Antarctic and Arctic (the former consisting of perennial land ice and the latter consisting of seasonally ice covered ocean) result in dramatically different net surface energy fluxes. In the Arctic, the seasonal cycles of $F_{\mathrm{SFC:NET}}$ and $F_{\mathrm{TOA:NET}}$ act to offset one another such that F_{WALL} has relatively little seasonal variation (Porter et al. 2010). In the Antarctic, however, the dominant balance throughout the year is between $F_{\mathrm{TOA:NET}}$ and F_{WALL}, with $F_{\mathrm{SFC:NET}}$ remaining comparatively small in magnitude (Fig. 2).

Comparing the solid (WACCM) and dashed lines (Part I estimate) in Fig. 2, one can see that WACCM captures the observed magnitude and seasonal variation of the Antarctic energy budget components quite well. In the annual mean, WACCM underestimates the magnitude of $F_{\mathrm{TOA:NET}}$ by ~7% and F_{WALL} by ~9%. WACCM overestimates the annual mean $F_{\mathrm{SFC:NET}}$ by ~33% (due to the small values of $F_{\mathrm{SFC:NET}}$). A detailed discussion of the biases in the WACCM Antarctic energy budget is included in appendix B, but we believe the model adequately serves our aim of studying past and future trends.

b. SAM variability

In the previous section, we demonstrated that WACCM successfully captures the climatological seasonal cycle

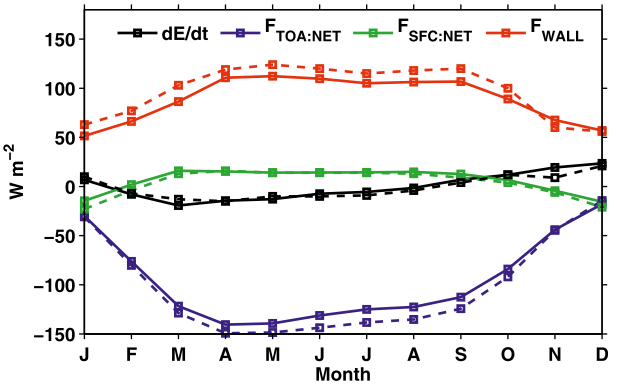

FIG. 2. 2001–10 climatological atmospheric energy budget components averaged over the polar cap (70°–90°S). The black, blue, green, and red solid curves respectively show the energy storage $\partial E/\partial t$, net top-of-atmosphere radiative flux $F_{\mathrm{TOA:NET}}$, the net surface radiative and turbulent fluxes $F_{\mathrm{SFC:NET}}$, and the horizontal energy flux convergence F_{WALL}. The dashed curves show the corresponding energy budget terms for the observational data for the same time period from Table 1 of Part I.

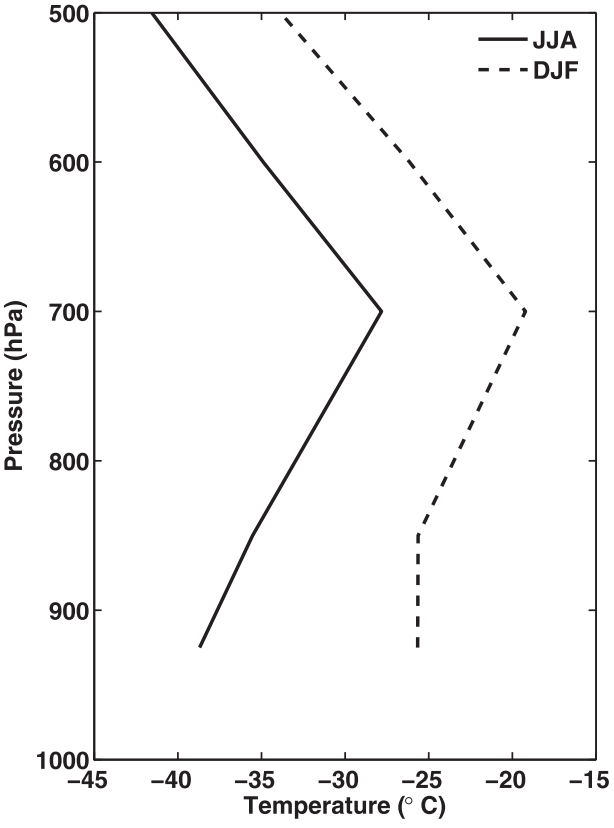

FIG. 3. Vertical profile of polar cap averaged (70°–90°S) temperature for June–August (JJA; solid curve) and DJF (dashed curve). Data points below the Antarctic surface are not included.

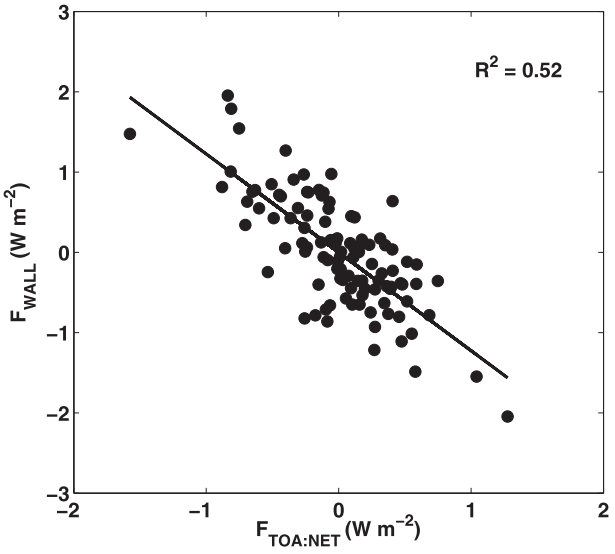

FIG. 4. Scatterplot of WACCM annual mean, piecewise, linearly detrended polar cap averaged (70°–90°S) $F_{\mathrm{TOA:NET}}$ and F_{WALL} anomalies for 1960–2065 (20C and 21C). Solid black line indicates the least squares linear fit to the data.

of the Antarctic energy budget, and is in good agreement with observations. We here turn to the interannual variability. Part I showed that the intraseasonal-to-interannual variability of the components of the energy budget is well correlated with large-scale modes of atmospheric variability, particularly the SAM. In this section, we continue our validation of the simulation of the Antarctic energy budget in WACCM by examining how well it simulates the interannual correlations with the SAM. Since the trend in the large-scale atmospheric circulation in the Southern Hemisphere during the twentieth-century period in WACCM is characterized by a positive trend in the SAM (Figs. 1b,c), it is important to validate the interannual relationships between energy budget components and the SAM in WACCM before we examine the trends.

First, we show that the horizontal energy flux convergence (F_{WALL}) and the net TOA radiative flux ($F_{\mathrm{TOA:NET}}$) not only balance each other in the climatological mean, but their detrended anomalies also balance. Figure 4 shows a scatterplot of the annual mean $F_{\mathrm{TOA:NET}}$ and F_{WALL} anomalies. In the annual mean, approximately 52% of the variance in F_{WALL} is explained by $F_{\mathrm{TOA:NET}}$. Thus, interannual changes in one component are coupled to changes in the other.

Second, we find that the observed annual mean correlations between the SAM and the energy budget components are well represented in WACCM. Figure 5 shows scatterplots of the annual mean $F_{\mathrm{TOA:NET}}$ (Fig. 5a), F_{WALL} (Fig. 5b), and $F_{\mathrm{SFC:NET}}$ (Fig. 5c) anomalies and the SAM. Note that the scale on the y axis in Fig. 5c is different from Figs. 5a and 5b. In the annual mean, the SAM is positively correlated with $F_{\mathrm{TOA:NET}}$ (primarily the LW flux; $R^2 = 0.48$), negatively correlated with F_{WALL} ($R^2 = 0.36$), and positively correlated with $F_{\mathrm{SFC:NET}}$ ($R^2 = 0.22$). These regressions are all significant at the 95% level and qualitatively agree with the observational equivalents discussed in Part I.

Third, we compare the seasonal correlations between the energy budget components and the SAM with Part I (see Table 2 herein). WACCM captures the sign and approximate magnitude of the correlations between $F_{\mathrm{TOA:SW}}$, $F_{\mathrm{TOA:LW}}$, and $F_{\mathrm{TOA:NET}}$ and the SAM in both June–August (JJA) and December–February (DJF) (cf. Table 2 of Part I). We note that the negative $F_{\mathrm{TOA:SW}}$–SAM correlation in DJF in WACCM arises primarily from the clear-sky component of $F_{\mathrm{TOA:SW}}$, and this is due in part to the negative correlation between total column ozone and the SAM during this season.

Broadly, the positive annual mean correlations between $F_{\mathrm{TOA:NET}}$ and the SAM reflect a decrease in outgoing LW radiation during the positive phase of the SAM

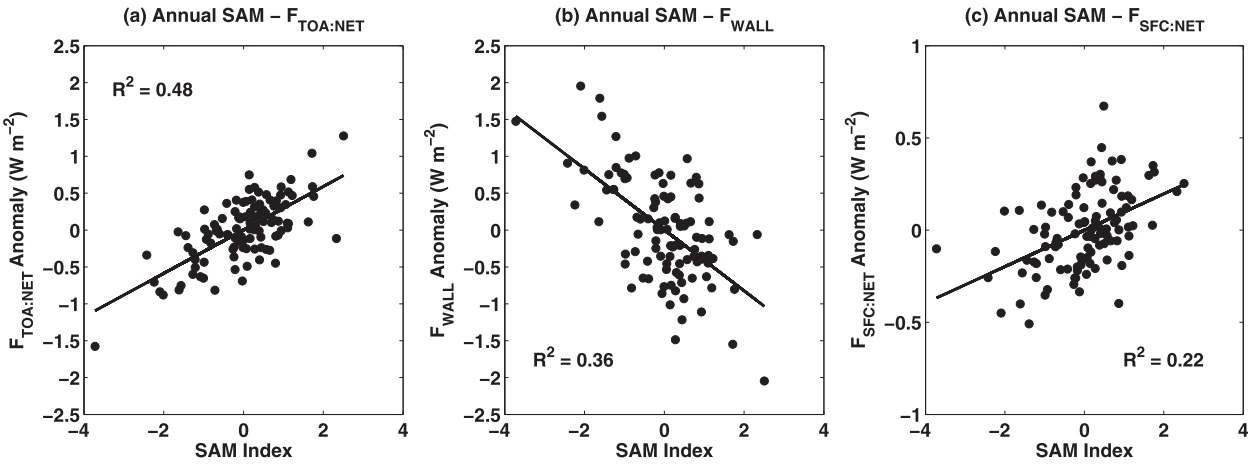

FIG. 5. Scatterplots of the WACCM annual mean, piecewise, linearly detrended SAM and the polar cap averaged (70°–90°S) (a) $F_{\mathrm{TOA:NET}}$, (b) F_{WALL}, and (c) $F_{\mathrm{SFC:NET}}$ anomalies for 1960–2065 (20C and 21C). Solid black lines indicate the least squares linear fit to the data. Note that the *y* axis in (c) differs from (a) and (b).

when the Antarctic continent is anomalously cold. In DJF, the positive correlation between $F_{\mathrm{TOA:LW}}$ and the SAM is offset by a negative correlation with $F_{\mathrm{TOA:SW}}$ (i.e., a decrease in absorbed solar radiation when the SAM is positive), which results in a weaker $F_{\mathrm{TOA:NET}}$–SAM correlation in DJF.

We also note several differences between the seasonal correlations in WACCM and in the observations (see Table 2 of Part I). Several of the differences are in the surface flux correlations that are the least constrained flux estimates in the observational energy budget of Part I (Berrisford et al. 2011). In the remainder of this section, we discuss the details of these differences.

In both DJF and JJA, we find positive correlations with $F_{\mathrm{SFC:SH+LH}}$ (primarily $F_{\mathrm{SFC:SH}}$) and the SAM. Part I also showed positive correlations in both seasons although the JJA correlation is not significant in the observations.

The SAM correlation with $F_{\mathrm{SFC:LW}}$ in JJA is also positive in WACCM but is insignificant in the observations. The sign of this correlation requires some clarification. There is a significant negative correlation between the *upward* $F_{\mathrm{SFC:LW}}$ and the SAM in JJA in WACCM, which agrees with the negative correlation between surface temperature and the SAM (not shown). However, there is also a negative correlation between the *downward* $F_{\mathrm{SFC:LW}}$ in JJA. The net effect is that the cooling of the atmospheric column during the positive phase of the SAM leads to a decrease in downward $F_{\mathrm{SFC:LW}}$ that exceeds the decrease in upward $F_{\mathrm{SFC:LW}}$. The cooling of the atmospheric column also explains the positive correlation in WACCM between $F_{\mathrm{SFC:SH+LH}}$ and the SAM in JJA due to a decrease in downward SH flux (Table 2). In the annual mean (Fig. 5c), the main contribution to the net surface flux is the net surface LW flux, $F_{\mathrm{SFC:LW}}$, and the explanation for the sign of the correlation is the same as the JJA correlation.

Finally, we find a negative correlation between F_{WALL} and the SAM in DJF and JJA in WACCM, again not present in the observations. This correlation implies that when the SAM is in its positive phase (i.e., the westerly jet is poleward shifted), the horizontal energy flux into Antarctica decreases. With respect to the two-way balance between F_{WALL} and $F_{\mathrm{TOA:NET}}$, these negative correlations in DJF and JJA agree with the positive $F_{\mathrm{TOA:NET}}$–SAM correlations in these seasons. They also agree with the sign of the annual mean correlation shown in Fig. 5b.

Overall, the annual mean relationships between the energy budget components and the SAM are well represented in WACCM, and Fig. 5 suggests that the relationships between the energy budget terms and the SAM in the annual mean are most representative of the relationships for JJA (Table 2). There are several seasonal

TABLE 2. DJF and JJA correlations between piecewise, linearly detrended Antarctic energy budget components and the SAM for 1960–2065 (20C and 21C). Bold font indicates correlations that are statistically significant at the 95% level.

	$\frac{\partial E}{\partial t}$	$F_{\mathrm{TOA:SW}}$	$F_{\mathrm{TOA:LW}}$	$F_{\mathrm{TOA:NET}}$	$F_{\mathrm{SFC:SW}}$	$F_{\mathrm{SFC:LW}}$	$F_{\mathrm{SFC:LH+SH}}$	$F_{\mathrm{SFC:NET}}$	F_{WALL}
DJF	−0.006	**−0.34**	**0.55**	**0.20**	0.14	0.11	**0.24**	**0.56**	**−0.26**
JJA	−0.10	0.12	**0.59**	**0.59**	−0.15	**0.39**	**0.28**	**0.46**	**−0.49**

differences in the SAM correlations between WACCM and the observations, and we note that these differences may be due in part to the short time series of the observational record (Table 2 of Part I used data for the 2001–10 time period only).

Having confirmed that our WACCM simulations generally capture both the mean and the variability of the Antarctic energy budget, in the next subsection we examine the recent past and projected future trends in the Antarctic energy budget. We will show that accounting for the direct effect of stratospheric ozone depletion and recovery on the radiative fluxes is crucial for interpreting the energy budget trends.

c. *Multidecadal trends: Ozone depletion and recovery*

As one can see from the black curves in Figs. 1b and 1c, the summertime and annual mean WACCM trends in the SAM during the twentieth-century period are positive. The largest positive trends occur in austral summer and are associated with springtime stratospheric ozone depletion, but weaker positive trends are also evident in winter and spring (not shown). Based on the above correlations between the SAM and the net TOA radiative flux ($F_{\mathrm{TOA:NET}}$) and the relationship between $F_{\mathrm{TOA:NET}}$ and the horizontal energy flux convergence, F_{WALL}, one might expect to find a contemporaneous positive trend in the annual mean $F_{\mathrm{TOA:NET}}$ and negative trend in F_{WALL} over this time period. Likewise, as the trend in the SAM is projected to change considerably in the future (21C), the trends in the energy budget components may be expected to change accordingly. However, this is not what we find in the WACCM simulations. The depletion and recovery of stratospheric ozone over the South Pole has a dramatic effect on $F_{\mathrm{TOA:SW}}$, and it completely overwhelms any effect that the SAM trends might have on trends in the energy budget components based on the relationships discussed in section 3b.

Figure 6a shows the time series of October–December averaged net TOA SW flux ($F_{\mathrm{TOA:SW}}$) in WACCM. OND is the season when stratospheric ozone depletion occurs over the South Pole. Note that $F_{\mathrm{TOA:SW}}$ decreases dramatically over the twentieth-century time period when ozone depletion occurs (cf. Fig. 1a). The decrease in net $F_{\mathrm{TOA:SW}}$ is due to the fact that less downward SW radiation is absorbed in the atmospheric column by stratospheric ozone and therefore more SW radiation reaches the clouds and the surface and is reflected back to space. Additionally, less of the reflected upward SW is absorbed in the stratosphere by the ozone layer. The result is an increase in upward SW and, thus, a decrease in net SW at the TOA ($F_{\mathrm{TOA:SW}}$). The largest contribution to the twentieth-century trend shown in Fig. 6a results from the clear-sky component of $F_{\mathrm{TOA:SW}}$ (not shown); however, the trend is slightly amplified (an $\sim$1 W m^{-2} decrease from 1960 to 2000) due to an increase

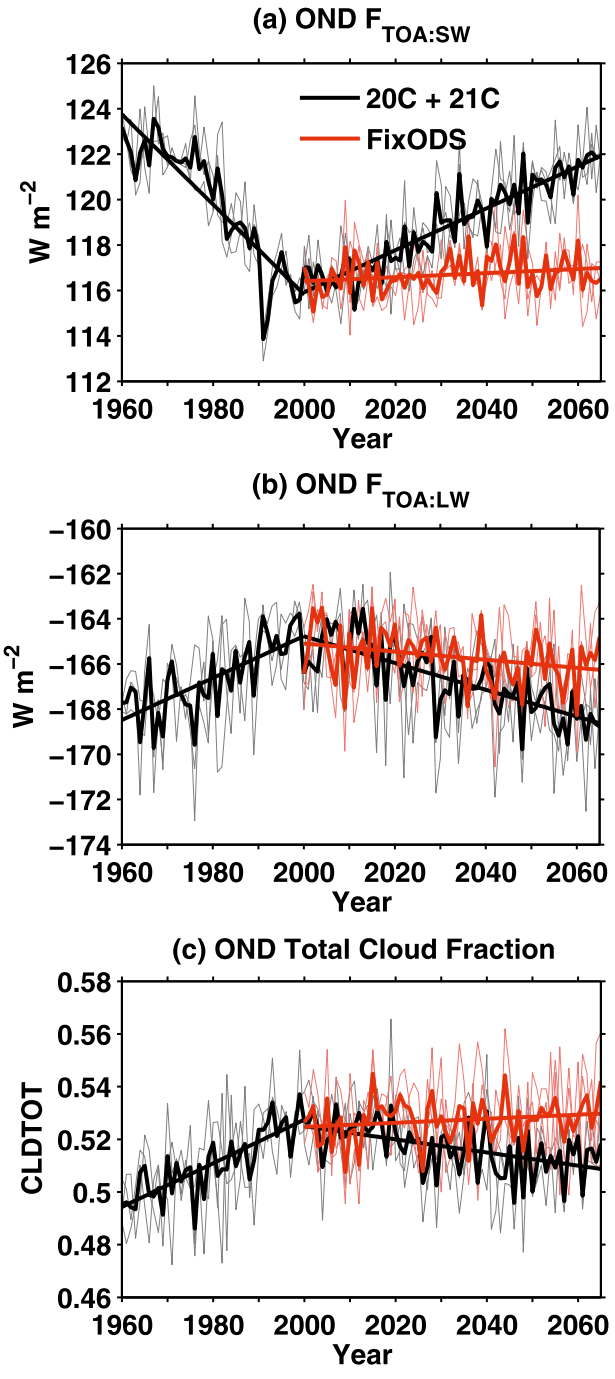

FIG. 6. WACCM time series of polar cap averaged OND (a) $F_{\mathrm{TOA:SW}}$, (b) $F_{\mathrm{TOA:LW}}$, and (c) total cloud fraction. Black curve indicates the 20C and 21C scenarios and red curve indicates the FixODS scenario. Least squares linear fits to 20C, 21C, and FixODS are shown. Individual ensemble members are shown in thin gray and pink curves.

in total cloud fraction during this time period, shown in Fig. 6c. The increase in total cloud fraction is associated with the poleward shift of the storm tracks. Note that the TOA SW trends are not associated with the positive trend

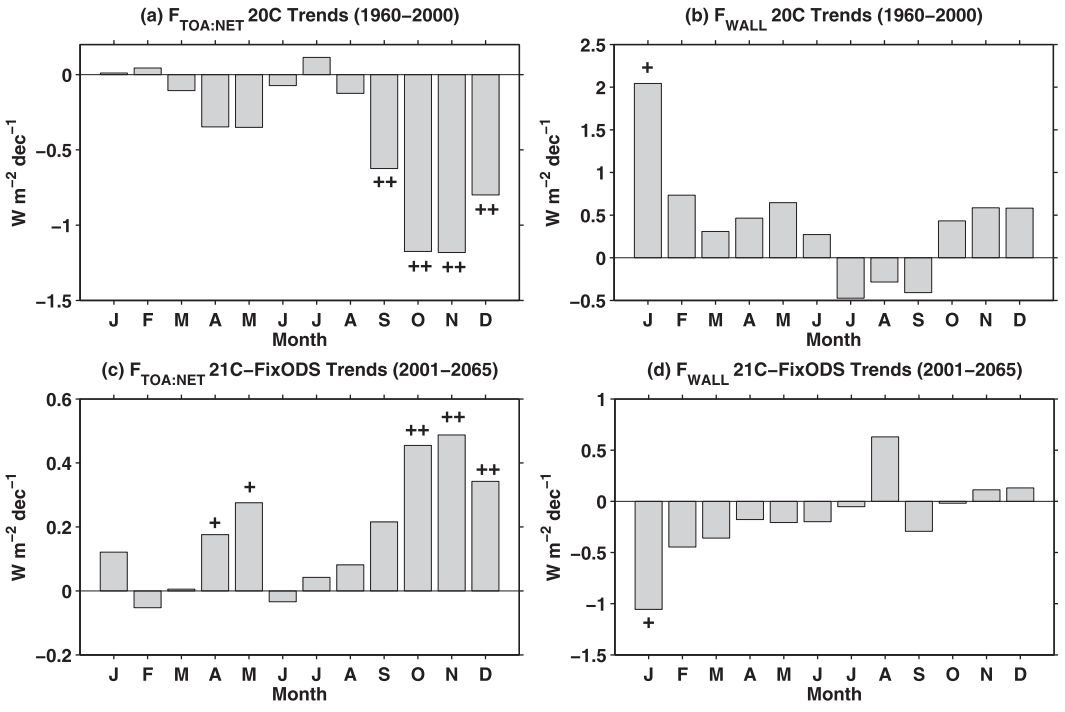

FIG. 7. Bar plots of monthly twentieth-century (20C) trends for polar cap averaged (70°–90°S) (a) $F_{TOA:NET}$ and (b) F_{WALL} in W m^{-2} decade^{-1}. (c),(d) As in (a),(b), but showing the difference in twenty-first century trends (21C − FixODS). Statistical significance is shown by the crosses (95%) and double crosses (99%).

in the SAM in OND as the detrended $F_{TOA:SW}$–SAM relationship in OND is not statistically significant (not shown). Overall, the interannual relationships between the energy budget components and the SAM in OND are very similar to those in JJA (see Table 2).

In the twenty-first century, $F_{TOA:SW}$ increases as ozone recovers in the 21C scenario, but remains relatively constant for the FixODS scenario (Fig. 6a). Total cloud fraction decreases slightly in the 21C scenario, complementing the effect of ozone recovery on $F_{TOA:SW}$, but changes little with FixODS (Fig. 6c). The only difference between our two twenty-first-century simulations is the prescribed surface concentrations of ODSs, and thus the difference in the twenty-first-century energy budget trends can be directly and unambiguously attributed to the differences in stratospheric ozone.

Figure 6b shows the time series of net TOA LW flux ($F_{TOA:LW}$) in OND in WACCM. Here $F_{TOA:LW}$ is also altered by the changes in stratospheric ozone. During the twentieth-century period, when ozone depletion occurs, $F_{TOA:LW}$ increases due to cooling of the stratosphere and the surface/troposphere (in accordance with the positive trend in the SAM). Greenhouse gas forcing also contributes to the cooling of the stratosphere. The increase in $F_{TOA:LW}$ is about half the magnitude of the decrease in $F_{TOA:SW}$ over the 1960–2000 time period, resulting in a pronounced negative $F_{TOA:NET}$ trend in OND (Fig. 7a). As ozone recovers (21C), $F_{TOA:LW}$ decreases, illustrating the combined warming of the stratosphere (due to ozone recovery) and the surface/troposphere (due to increases in GHG). For the FixODS scenario, the surface/troposphere warms but the stratosphere continues to cool, causing a weaker decrease in $F_{TOA:LW}$.

The key role of ozone depletion and recovery is brought to light by considering the seasonal cycle of the trends in the twentieth- and twenty-first-century periods. Figure 7a shows the monthly twentieth-century trends for $F_{TOA:NET}$ in WACCM. Negative trends are statistically significant in austral spring, as one might expect. During the twentieth-century period, $F_{TOA:NET}$ decreases because of the decrease in $F_{TOA:SW}$. Note that the detrended, interannual $F_{TOA:NET}$–SAM correlation in OND is positive and statistically significant (not shown), suggesting that a positive trend in the SAM in OND cannot explain the negative trends in $F_{TOA:NET}$ in Fig. 7a.

In the twenty-first century, for the 21C scenario, the increase in $F_{TOA:SW}$ results in a positive trend in $F_{TOA:NET}$ in austral spring, whereas for the FixODS scenario the decrease in $F_{TOA:LW}$ leads to a weak negative trend in $F_{TOA:NET}$ in spring. This is shown in the differences (21C − FixODS) between the $F_{TOA:NET}$ trends in the twenty-first century (Fig. 7c). The differences are positive

and statistically significant at the 95% level in OND. The statistically significant $F_{\mathrm{TOA:NET}}$ trend differences in April and May reflect two processes; first, ozone recovery from an approximate 15% loss occurs in these months, which leads to increased absorbed SW radiation, and second, significant sea ice loss near the continent in the FixODS scenario relative to the 21C scenario leads to enhanced warming near the Antarctic coast (see Fig. 3b of Smith et al. 2012) and increased outgoing LW radiation. Studies have shown that the climate effects of independently prescribed GHG forcing and ozone recovery in GCMs are approximately additive (Polvani et al. 2011a; McLandress et al. 2011); thus, the effect of GHG forcing on $F_{\mathrm{TOA:NET}}$ roughly subtracts out in Fig. 7c.

For both the twentieth- and twenty-first-century periods, the trends in OND $F_{\mathrm{TOA:NET}}$ are evident in like-signed trends in the energy tendency, $\partial E/\partial t$, for the same season (not shown). Notably, these trends in $F_{\mathrm{TOA:NET}}$ coincide with opposite-signed trends in the SAM, particularly in December. In other words, the positive interannual correlation between the SAM and $F_{\mathrm{TOA:NET}}$ described in section 3b is nowhere to be seen in the trends. Again, this shows that stratospheric ozone is the controlling factor, and the SAM does not give useful information about long-term trends (contrast Figs. 1b and 7a,c).

Having examined $F_{\mathrm{TOA:NET}}$, we now turn to the horizontal energy flux convergence, F_{WALL}. Figure 7b shows the monthly twentieth-century trends for F_{WALL} in WACCM. Austral summer is the season that experiences the largest positive trends in F_{WALL}, particularly in January when the trend is statistically significant at the 95% level. Note that while the trend in F_{WALL} is positive, there is also a positive trend in the SAM in summer during the twentieth-century period (Fig. 1b) that runs counter to the interannual relationship between the summer SAM and F_{WALL} shown in Table 2. Although an investigation of the dynamical mechanisms that drive the trends in F_{WALL} is beyond the scope of this paper, it is clear that the trends in F_{WALL} act to compensate for the trends in $F_{\mathrm{TOA:NET}}$ one to two months earlier.

In the twenty-first century, the trend in F_{WALL} reverses sign in summer as ozone recovers and is weakly positive for the FixODS scenario (not shown). The differences between the F_{WALL} trends in the two twenty-first-century scenarios (21C − FixODS) are shown in Fig. 7d and are statistically significant at the 95% level in January. For both the twentieth- and twenty-first-century scenarios, the F_{WALL} trends are reflected in like-signed trends in $\partial E/\partial t$ during the summer season (not shown).

As for the net surface flux ($F_{\mathrm{SFC:NET}}$), there are no significant trends in the 20C, 21C, or FixODS simulations in any month (not shown). This further demonstrates that the two-way balance between $F_{\mathrm{TOA:NET}}$ and F_{WALL} in the Antarctic region found in the climatological mean and on intraseasonal-to-interannual time scales also carries over to the multidecadal time scale changes considered here. This balance, characteristic of the Antarctic and very much unlike the Arctic, appears to hold on all time scales.

Finally, the annual mean trends in the Antarctic atmospheric energy budget are shown in Fig. 8. The annual mean time series of $F_{\mathrm{TOA:NET}}$ (Fig. 8a) shows a negative trend during the decades of ozone depletion. In the twenty-first century as ozone recovers (21C), there is very little trend in $F_{\mathrm{TOA:NET}}$ due to opposite-signed trends in $F_{\mathrm{TOA:LW}}$ and $F_{\mathrm{TOA:SW}}$, with the SW changes being confined to the OND season and the LW changes occurring throughout the year. The effect of future GHG forcing alone on the annual mean $F_{\mathrm{TOA:NET}}$ is clearly seen in the FixODS scenario, indicating a weak but significant negative trend due to increased outgoing LW radiation.

Figure 8b shows the annual mean time series of F_{WALL}. During the twentieth-century period, the negative trend in $F_{\mathrm{TOA:NET}}$ (Fig. 8a) is balanced by a positive trend in F_{WALL}. For the 21C scenario, Fig. 8b depicts a relatively flat trend, consistent with the weak trend in $F_{\mathrm{TOA:NET}}$ for the same scenario. For the FixODS scenario, which represents the effect of GHG forcing alone, a positive F_{WALL} trend balances the negative trend in $F_{\mathrm{TOA:NET}}$. Thus, Fig. 8 suggests that projected ozone recovery mitigates the increase in horizontal energy flux into the Antarctic polar cap associated with GHG warming.

4. Summary and conclusions

In this paper, we have extended our examination of the Antarctic atmospheric energy budget using an ensemble of integrations of the CESM1(WACCM) climate model. We find that WACCM reproduces the climatological energy budget reasonably well relative to the observational estimate presented in Part I. In addition, we have shown that WACCM is able to capture the observed interannual relationships between the energy budget terms and the SAM. A large fraction of the interannual variability in the energy budget terms can be explained by the SAM, particularly in austral winter. In the annual mean, the net TOA radiative flux, $F_{\mathrm{TOA:NET}}$, and the horizontal energy flux convergence, F_{WALL}, are positively and negatively correlated with the SAM, respectively.

From an energy balance perspective, the opposite-signed interannual correlations reflect the fact that, seasonally and in the annual mean, energy balance over the Antarctic polar cap is primarily satisfied through compensating changes in F_{WALL} and $F_{\mathrm{TOA:NET}}$. From a

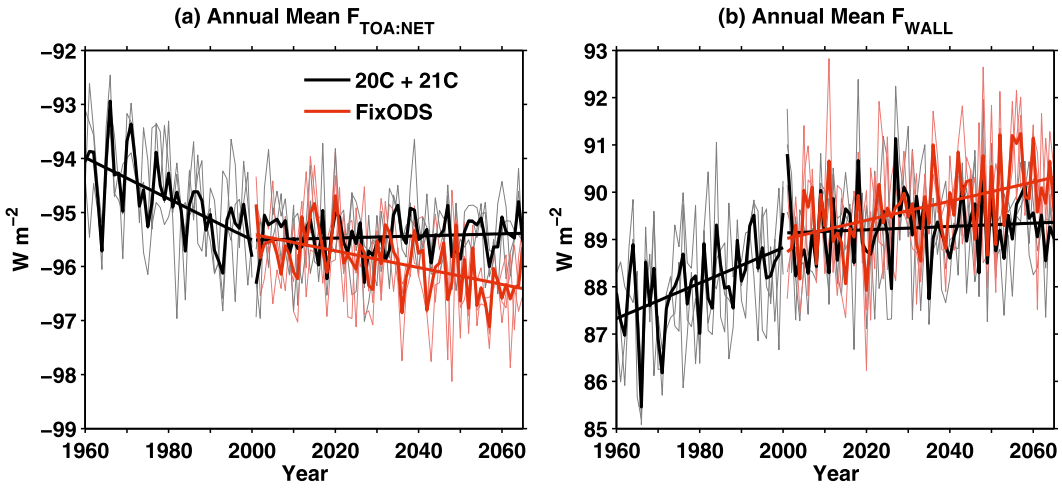

FIG. 8. As in Fig. 6, but for annual mean (a) $F_{\mathrm{TOA:NET}}$ and (b) F_{WALL}.

dynamical perspective, however, the negative correlation between F_{WALL} and the SAM might seem counterintuitive. During the positive phase of the SAM the baroclinic zone is shifted poleward and one would naively guess this would result in larger energy flux into the polar cap by synoptic eddies; yet the opposite is found in both WACCM and the reanalysis (Part I). Weaker energy flux during the positive phase of the SAM suggests that synoptic eddies may become less efficient at transporting energy with a poleward-displaced baroclinic zone (Carleton and Whalley 1988). This dynamical interpretation is complicated, however, by the fact that the twentieth-century summertime trend in F_{WALL} is *positive* when the SAM is trending positive and the westerly jet is shifting poleward. Our investigation of the nature of the relationship between F_{WALL} and the SAM is ongoing.

On multidecadal time scales, the effects of ozone depletion and projected recovery dominate the trends in the Antarctic energy budget from 1960 to 2065. During the twentieth-century period from 1960 to 2000, ozone depletion results in an annual mean decrease in $F_{\mathrm{TOA:NET}}$ due to the decrease in $F_{\mathrm{TOA:SW}}$. This is balanced by an increase in F_{WALL}. In the twenty-first century as ozone recovers, the opposite-signed trends in the net TOA SW and LW fluxes ($F_{\mathrm{TOA:SW}}$ and $F_{\mathrm{TOA:LW}}$) result in little trend in $F_{\mathrm{TOA:NET}}$ and consequently F_{WALL}. An alternative twenty-first-century scenario in which GHG warming occurs in the absence of ozone recovery shows a continued increase in F_{WALL} in the future. Thus, the future positive trend in energy flux convergence into the Antarctic polar cap due to GHG warming is mitigated by ozone recovery.

This study highlights the fact that the annual mean interannual correlations between the SAM and $F_{\mathrm{TOA:NET}}$ and F_{WALL} do not help to explain the multidecadal trends in these fluxes. Smith et al. (2012) arrived at a similar conclusion with respect to the SAM and Antarctic sea ice trends. Although the SAM is a good predictor of interannual variations in Antarctic climate, we emphasize that the SAM may not be a good predictor of multidecadal trends in the Antarctic climate system and we caution against using the SAM as a means of explaining trends.

The role of energy flux convergence in future Antarctic polar amplification is currently unknown. As GCMs do not yet include dynamic Antarctic ice sheet and ice shelf components, it is unclear how increases in well-mixed GHGs and ozone recovery will affect the Antarctic surface energy balance in the future and how changes in the surface energy balance will be compensated for by changes in other components of the Antarctic atmospheric energy budget. Our WACCM simulations show no statistically significant trend in $F_{\mathrm{SFC:NET}}$ in either the 21C or FixODS twenty-first-century scenarios. Despite current model limitations, our work suggests that the effect of ozone recovery in the future may mask the effect of GHG warming on the Antarctic energy budget for several decades.

Acknowledgments. The authors would like to gratefully acknowledge the NSF Antarctic Sciences Program, ANT-09-44063. The CESM Project is supported by the National Science Foundation (NSF) and the Office of Science (BER) of the U.S. Department of Energy. All model integrations were performed at the National Center for Atmospheric Research (NCAR), which is sponsored by the U.S. NSF. We thank Dan Marsh, Mike Mills, and Doug Kinnison at NCAR for their assistance with the model integrations.

APPENDIX A

Vertically Integrated Atmospheric Energy Budget Derivation

Some of the steps needed to obtain Eqs. (1)–(5) are mentioned in the literature (e.g., Trenberth and Solomon 1994; Trenberth 1997). However, we were unable to find a complete and coherent derivation of these equations from first principles. Hence, for the sake of completeness, we include it here with enough detail to make the derivation easily understandable. We start with the thermodynamic equation,

$$c_p\left[\frac{\partial T}{\partial t}+\mathbf{v}\cdot\nabla T+\omega\left(\frac{\partial T}{\partial p}-\kappa\frac{T}{p}\right)\right]=Q, \qquad \text{(A1)}$$

where T is temperature, $\mathbf{v}$ is the horizontal wind vector, ω is the vertical wind component, p is pressure, c_p is the isobaric specific heat capacity, κ is the ratio of the specific gas constant, R, to c_p, and Q is the diabatic heating. The kinetic energy equation is obtained by taking the dot product of the horizontal momentum equations with $\mathbf{v}$,

$$\frac{\partial k}{\partial t}+\nabla\cdot k\mathbf{v}+\frac{\partial k\omega}{\partial p}=-\mathbf{v}\cdot\nabla\Phi+\mathbf{v}\cdot\mathbf{F}, \qquad \text{(A2)}$$

where k is the kinetic energy, Φ is the geopotential, and $\mathbf{F}$ is friction. Neglecting frictional dissipation and using the ideal gas law, the hydrostatic equation and the continuity equation, the sum of Eqs. (A1) and (A2) can be written as

$$\frac{\partial(c_pT+k)}{\partial t}+\nabla\cdot(c_pT+\Phi+k)\mathbf{v}+\frac{\partial(c_pT+\Phi+k)\omega}{\partial p}=Q. \qquad \text{(A3)}$$

Next, we add the moisture equation to Eq. (A3) to obtain

$$\frac{\partial(c_pT+k+Lq)}{\partial t}+\nabla\cdot(c_pT+\Phi+k+Lq)\mathbf{v}+\frac{\partial(c_pT+\Phi+k+Lq)\omega}{\partial p}=Q+L(e-c), \qquad \text{(A4)}$$

where q is the specific humidity, L is the latent heat of vaporization for water, e is the rate of evaporation, and c is the rate of condensation within the atmosphere per unit mass. Now, we vertically integrate Eq. (A4) and use the Leibniz rule to take $\partial/\partial t$ and $\nabla\cdot$ outside of the integrals. The terms on the left-hand side of Eq. (A4) become

$$\int_0^{p_s}\frac{\partial(c_pT+k+Lq)}{\partial t}\frac{dp}{g}=\frac{\partial}{\partial t}\int_0^{p_s}(c_pT+k+Lq)\frac{dp}{g}-\frac{1}{g}(c_pT+k+Lq)|_{p_s}\frac{\partial p_s}{\partial t}, \qquad \text{(A5)}$$

$$\int_0^{p_s}\nabla\cdot(c_pT+\Phi+k+Lq)\mathbf{v}\frac{dp}{g}=\nabla\cdot\int_0^{p_s}(c_pT+\Phi+k+Lq)\mathbf{v}\frac{dp}{g}-\frac{1}{g}(c_pT+\Phi+k+Lq)\mathbf{v}|_{p_s}\cdot\nabla p_s, \qquad \text{(A6)}$$

and

$$\int_0^{p_s}\frac{\partial(c_pT+\Phi+k+Lq)}{\partial p}\frac{dp}{g}=\frac{1}{g}(c_pT+\Phi+k+Lq)\omega|_{p_s}, \qquad \text{(A7)}$$

where subscript s indicates the surface value. To reduce these terms to the form outlined in section 2b, we use the definition of ω evaluated at the surface,

$$\omega_s=\frac{\partial p_s}{\partial t}+\mathbf{v}_s\cdot\nabla p_s. \qquad \text{(A8)}$$

Substituting ω_s in Eq. (A7) for Eq. (A8), and substituting Eqs. (A5)–(A7) in the vertically integrated Eq. (A4), many of the terms cancel and we end up with

$$\frac{\partial}{\partial t}\int_0^{p_s}(c_pT+k+Lq)\frac{dp}{g}+\nabla\cdot\int_0^{p_s}(c_pT+\Phi+k+Lq)\mathbf{v}\frac{dp}{g}-\frac{1}{g}\Phi_s\mathbf{v}_s\cdot\nabla p_s+\frac{1}{g}\Phi_s\omega_s=\int_0^{p_s}[Q+L(e-c)]\frac{dp}{g}. \qquad \text{(A9)}$$

Substituting Eq. (A8) into Eq. (A9), and rearranging the partial derivatives, we get

$$\frac{\partial}{\partial t}\int_0^{p_s}(c_pT+k+Lq)\frac{dp}{g}+\nabla\cdot\int_0^{p_s}(c_pT+\Phi+k+Lq)\mathbf{v}\frac{dp}{g}+\frac{1}{g}\frac{\partial p_s\Phi_s}{\partial t}=\int_0^{p_s}[Q+L(e-c)]\frac{dp}{g}. \qquad \text{(A10)}$$

Finally, taking the $\partial p_s\Phi_s/\partial t$ inside the integral gives

$$\frac{\partial}{\partial t}\int_0^{p_s}(c_pT + k + Lq + \Phi_s)\frac{dp}{g} + \nabla\cdot\int_0^{p_s}(c_pT + \Phi + k + Lq)\mathbf{v}\frac{dp}{g} = \int_0^{p_s}[Q + L(e-c)]\frac{dp}{g}. \quad \text{(A11)}$$

The left-hand side of Eq. (A11) is now in the form shown in section 2b. The right-hand side of Eq. (A11) can be rewritten as

$$\int_0^{p_s}[Q + L(e-c)]\frac{dp}{g} = F_{\text{TOA:NET}} + F_{\text{SFC:RAD}} + F_{\text{SFC:SH}} + LP + L(E-P), \quad \text{(A12)}$$

where $F_{\text{TOA:NET}}$ is the net radiative flux at the top of the atmosphere, $F_{\text{SFC:}RAD}$ is the net radiative flux at the surface, $F_{\text{SFC:SH}}$ is the surface sensible heat flux, and P and E are the precipitation and the surface evaporation rates; LE is equivalent to the surface latent heat flux, $F_{\text{SFC:LH}}$. Thus, the complete energy budget equation as outlined in section 2b is as follows:

$$\frac{\partial}{\partial t}\int_0^{p_s}(c_pT + k + Lq + \Phi_s)\frac{dp}{g} + \nabla\cdot\int_0^{p_s}(c_pT + \Phi + k + Lq)\mathbf{v}\frac{dp}{g} = F_{\text{TOA:NET}} + F_{\text{SFC:NET}}, \quad \text{(A13)}$$

where $F_{\text{TOA:NET}}$ and $F_{\text{SFC:NET}}$ are as defined in Eqs. (3) and (4) in section 2b.

APPENDIX B

Antarctic Atmospheric Energy Budget Biases in WACCM

a. Data

We use several observational data products to examine the biases in the Antarctic atmospheric energy budget in WACCM. We use the CERES satellite data of TOA radiative fluxes from 2001 to 2010. Monthly CERES TOA fluxes from the Energy Balanced and Filled (EBAF) dataset are obtained on a 1° × 1° grid from the National Aeronautics and Space Administration (NASA) Langley Research Center Atmospheric Science Data Center. To produce the EBAF data, CERES TOA shortwave (SW) and longwave (LW) fluxes are adjusted such that the global mean net TOA flux (averaged over several years) is equal to the estimated present-day change in heat storage in the Earth system (Loeb et al. 2009). This procedure thus eliminates the unrealistically large global mean TOA flux that exists in the unadjusted CERES data (Trenberth et al. 2009). We also use the associated computed CERES surface radiative flux product for 2001–10 (Kratz et al. 2010).

To assess the model-simulated cloud cover, we use satellite-derived total cloud fraction and cloud mean water path from the International Satellite Cloud Climatology Project (ISCCP), which provides complete spatial coverage of the Antarctic polar cap (Rossow and Schiffer 1999). Climatological monthly mean ISCCP fields based on data from July 1983 to December 2009 are obtained on a 2.5° × 2.5° grid from the NASA Goddard Institute for Space Studies.

Column ozone in WACCM is compared to the AC&C/SPARC (expansion below) ozone database for 2001–09. This database was created as a joint effort between the Chemistry–Climate Modeling Validation (CCMVal) Activity of the World Meteorological Organization's Stratospheric Processes and their Role in Climate (SPARC) project and the Atmospheric Chemistry and Climate (AC&C) Initiative, for use as a forcing for CMIP5 general circulation models (GCMs) that do not include interactive ozone chemistry (Cionni et al. 2011). For 2001–09, the AC&C/SPARC stratospheric ozone database is generated in a manner similar to Randel and Wu (2007).

Lastly, we compare WACCM surface air temperature (SAT) for 2001–10 to observations from 18 Antarctic weather stations (see Fig. 1 in Part I). These observations were made available as part of the Reference Antarctic Data for Environmental Research (READER) project (Turner and Colwell 2004).

b. Model biases

Figure B1a shows the TOA biases in WACCM relative to CERES for the 2001–10 period. The blue curve shows the $F_{\text{TOA:NET}}$ bias relative to CERES, which is positive throughout the year except in December. The positive bias in $F_{\text{TOA:NET}}$ arises primarily from the positive bias in the $F_{\text{TOA:LW}}$ component, while the negative $F_{\text{TOA:NET}}$ bias in December arises from the negative bias in $F_{\text{TOA:SW}}$ (solid red curve).

In general, there is no consensus on the sign of $F_{\text{TOA:LW}}$ biases in the Antarctic across reanalyses and GCMs (Trenberth and Fasullo 2010). The positive bias in WACCM is mainly due to the cold SAT bias in WACCM over the Antarctic region. Figure B1b (black curve) shows the WACCM SAT relative to Antarctic station data from READER (see Fig. 1 of Part I for station locations). The seasonal cycle of the WACCM $F_{\text{TOA:LW}}$ bias (Fig. 9a) generally agrees with the SAT bias.

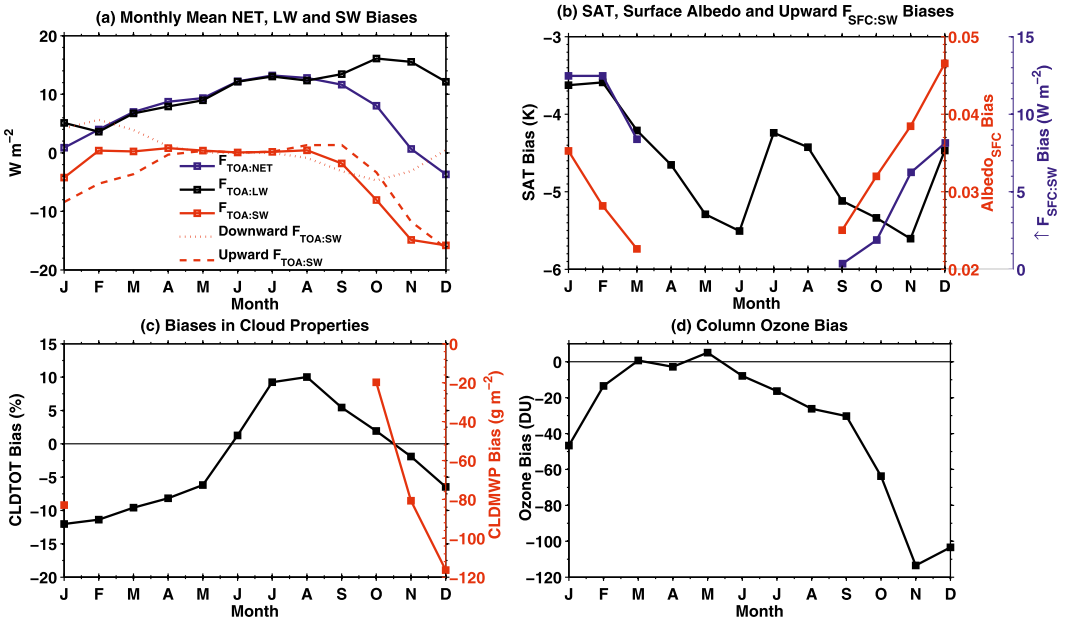

FIG. B1. (a) 2001–10 WACCM biases in top-of-atmosphere radiative fluxes (i.e., WACCM minus CERES). The solid blue, black, and red curves show the $F_{TOA:NET}$ bias, $F_{TOA:LW}$ bias, and $F_{TOA:SW}$ bias relative to CERES. The dotted and dashed red curves show the downward and upward components of the $F_{TOA:SW}$ bias relative to CERES. (b) 2001–10 WACCM biases in surface air temperature (SAT) relative to Antarctic station data (black curve), polar cap averaged (70°–90°S) surface albedo relative to CERES (red curve), and polar cap averaged (70°–90°S) upward $F_{SFC:SW}$ relative to CERES (blue curve). To calculate the SAT bias, the nearest WACCM grid point to each READER station was selected and the SAT bias was averaged over all selected grid points. (c) 1983–2009 WACCM biases in total cloud fraction, CLDTOT (black curve), and total cloud mean water path, CLDMWP (red curve), relative to ISCCP. (d) 2001–09 WACCM bias in column ozone (polar cap averaged and vertically integrated from 500 to 1 hPa) relative to the AC&C/SPARC ozone database.

In addition to the surface air temperature bias, WACCM displays a negative stratospheric ozone bias (Fig. B1d; polar cap averaged (70°–90°S) and column integrated between 500 and 1 hPa) relative to the AC&C/SPARC ozone database for the time period 2001–09. The ozone bias may also be contributing to the positive $F_{TOA:LW}$ bias in WACCM, particularly in austral spring. A negative bias in ozone cools the stratosphere due to a decrease in absorption of SW radiation. Indeed, the lower stratosphere in WACCM is known to be biased cold (Marsh et al. 2013). The AC&C/SPARC ozone database is constructed using satellite and ozonesonde data and may itself be biased somewhat high in the Antarctic relative to other observationally based ozone climatologies (Hassler et al. 2012).

The SW biases in WACCM (Fig. B1a) are not typical of reanalyses and GCMs (Trenberth and Fasullo 2010). Trenberth and Fasullo (2010) show that reanalyses and GCMs typically overestimate $F_{TOA:SW}$ at high southern latitudes. In contrast, WACCM underestimates $F_{TOA:SW}$, particularly in austral spring and summer. The Community Climate System Model version 3 (CCSM3) was also shown to underestimate $F_{TOA:SW}$ over the Antarctic polar cap (Briegleb and Bromwich 1998). In fall, a negative WACCM bias in upward $F_{TOA:SW}$ is partially offset by a positive bias in downward solar flux in WACCM relative to CERES (dotted red curve, Fig. B1a). In spring, a fraction of the negative WACCM bias in $F_{TOA:SW}$ can be attributed to too little downward solar flux at the top of the atmosphere. The remainder of the negative bias is explained by the fact that WACCM is reflecting more SW radiation from the surface and atmosphere back to space compared to CERES (dashed red curve, Fig. B1a). We attribute this to WACCM's positive bias in surface albedo (Fig. B1b) and negative bias in stratospheric ozone (Fig. B1d).

Figure B1b shows WACCM's polar cap averaged surface albedo bias relative to CERES (red curve). During polar night, we are unable to get a reliable estimate of the surface albedo from CERES SW fluxes. The WACCM bias in surface albedo results in a positive bias in upward $F_{SFC:SW}$ in the model (Fig. B1b, blue curve). To verify that the $F_{TOA:SW}$ bias is not directly related to biases in the simulated cloud fields, we plot the WACCM biases in total cloud amount (CLDTOT) and cloud mean water path (CLDMWP) relative to ISCCP in Fig. B1c. It

is important to note that there are challenges when comparing model-simulated cloud data with satellite-derived data, particularly in polar regions where satellite products contain significant biases (Bromwich et al. 2012). For example, ISCCP, which is based on passive visible–infrared (VIS-IR) retrievals, is missing CLDMWP information at high latitudes from February through September due to very low insolation during these months.

Unlike the CMIP3 models and CCSM3, which typically overestimate cloud amount over the Antarctic polar cap throughout the year (Bromwich et al. 2012; Briegleb and Bromwich 1998), WACCM tends to underestimate cloud amount in late spring, summer, and fall and overestimate in winter and early spring. When the $F_{\mathrm{TOA:SW}}$ bias is largest in late austral spring, WACCM has negative biases in both CLDTOT and CLDMWP (Fig. B1c). This indicates that the negative bias in $F_{\mathrm{TOA:SW}}$ is likely not due to increased SW reflection back to space due to a greater amount of brighter clouds in WACCM. In fact, the negative biases in cloud properties in WACCM act to amplify the effect of the surface albedo bias on the $F_{\mathrm{TOA:SW}}$ bias. A detailed analysis of the cloud properties in WACCM is beyond the scope of this study.

The negative bias in stratospheric ozone may also contribute to the negative $F_{\mathrm{TOA:SW}}$ bias in WACCM. A negative bias in ozone indicates that less SW radiation is absorbed by ozone and is therefore available to be reflected back to space by the surface, clouds, and atmosphere.

REFERENCES

Berrisford, P., P. Kållberg, S. Kobayashi, D. Dee, S. Uppala, A. J. Simmons, P. Poli, and H. Sato, 2011: Atmospheric conservation properties in ERA-Interim. *Quart. J. Roy. Meteor. Soc.,* **137,** 1381–1399, doi:10.1002/qj.864.

Briegleb, B., and D. Bromwich, 1998: Polar radiation budgets of the NCAR CCM3. *J. Climate,* **11,** 1246–1269.

Bromwich, D., and Coauthors, 2012: Tropospheric clouds in Antarctica. *Rev. Geophys.,* **50,** RG1004, doi:10.1029/2011RG000363.

Carleton, A., and D. Whalley, 1988: Eddy transport of sensible heat and the life history of synoptic systems: A statistical analysis for the Southern Hemisphere winter. *Meteor. Atmos. Phys.,* **38,** 140–152.

Cionni, I., and Coauthors, 2011: Ozone database in support of CMIP5 simulations: Results and corresponding radiative forcing. *Atmos. Chem. Phys.,* **11,** 11 267–11 292, doi:10.5194/acp-11-11267-2011.

Cullather, R. I., and M. G. Bosilovich, 2012: The energy budget of the polar atmosphere in MERRA. *J. Climate,* **25,** 5–24.

Dee, D. P., and Coauthors, 2011: The ERA-Interim reanalysis: Configuration and performance of the data assimilation system. *Quart. J. Roy. Meteor. Soc.,* **137,** 553–597, doi:10.1002/qj.828.

Fasullo, J. T., and K. E. Trenberth, 2008: The annual cycle of the energy budget. Part II: Meridional structures and poleward transports. *J. Climate,* **21,** 2313–2325.

Gent, P. R., and Coauthors, 2011: The Community Climate System Model version 4. *J. Climate,* **24,** 4973–4991.

Genthon, C., and G. Krinner, 1998: Convergence and disposal of energy and moisture on the Antarctic polar cap from ECMWF reanalyses and forecasts. *J. Climate,* **11,** 1703–1716.

Hassler, B., P. J. Young, R. W. Portmann, G. E. Bodeker, J. S. Daniel, K. H. Rosenlof, and S. Solomon, 2012: Comparison of three vertically resolved ozone data bases: Climatology, trends and radiative forcings. *Atmos. Chem. Phys. Discuss.,* **12,** 26 561–26 605, doi:10.5194/acpd-12-26561-2012.

Kang, S. M., L. M. Polvani, J. C. Fyfe, and M. Sigmond, 2011: Impact of polar ozone depletion on subtropical precipitation. *Science,* **332,** 951–954, doi:10.1126/science.1202131.

Kay, J. E., M. M. Holland, C. M. Bitz, E. Blanchard-Wrigglesworth, A. Gettelman, A. Conley, and D. Bailey, 2012: The influence of local feedbacks and northward heat transport on the equilibrium Arctic climate response to increased greenhouse gas forcing. *J. Climate,* **25,** 5433–5450.

Kistler, R., E. Kalnay, and W. Collins, 2001: The NCEP–NCAR 50-Year Reanalysis: Monthly means CD-ROM and documentation. *Bull. Amer. Meteor. Soc.,* **82,** 247–267.

Kratz, D. P., S. K. Gupta, A. C. Wilber, and V. E. Sothcott, 2010: Validation of the CERES edition 2B surface-only flux algorithms. *J. Appl. Meteor. Climatol.,* **49,** 164–180.

Lee, S., and S. B. Feldstein, 2013: Detecting ozone- and greenhouse gas–driven wind trends with observational data. *Science,* **339,** 563–567, doi:10.1126/science.1225154.

Loeb, N. G., B. A. Wielicki, D. R. Doelling, G. L. Smith, D. F. Keyes, S. Kato, N. Manalo-Smith, and T. Wong, 2009: Toward optimal closure of the earth's top-of-atmosphere radiation budget. *J. Climate,* **22,** 748–766.

Marsh, D. R., M. J. Mills, D. E. Kinnison, J.-F. Lamarque, N. Calvo, and L. M. Polvani, 2013: Climate change from 1850 to 2005 simulated in CESM1(WACCM). *J. Climate,* **26**, 7372–7391.

Marshall, G., 2003: Trends in the southern annular mode from observations and reanalyses. *J. Climate,* **16,** 4134–4143.

McLandress, C., T. G. Shepherd, J. F. Scinocca, D. A. Plummer, M. Sigmond, A. I. Jonsson, and M. C. Reader, 2011: Separating the dynamical effects of climate change and ozone depletion. Part II: Southern Hemisphere troposphere. *J. Climate,* **24,** 1850–1868.

Meinshausen, M., and Coauthors, 2011: The RCP greenhouse gas concentrations and their extensions from 1765 to 2300. *Climatic Change,* **109,** 213–241, doi:10.1007/s10584-011-0156-z.

Nakamura, N., and A. Oort, 1988: Atmospheric heat budgets of the polar regions. *J. Geophys. Res.,* **93** (D8), 9510–9524.

Polvani, L. M., M. Previdi, and C. Deser, 2011a: Large cancellation, due to ozone recovery, of future Southern Hemisphere atmospheric circulation trends. *Geophys. Res. Lett.,* **38,** L04707, doi:10.1029/2011GL046712.

——, D. W. Waugh, G. J. P. Correa, and S.-W. Son, 2011b: Stratospheric ozone depletion: The main driver of twentieth-century atmospheric circulation changes in the Southern Hemisphere. *J. Climate,* **24,** 795–812.

Porter, D. F., J. J. Cassano, M. C. Serreze, and D. N. Kindig, 2010: New estimates of the large-scale Arctic atmospheric energy budget. *J. Geophys. Res.,* **115,** D08108, doi:10.1029/2009JD012653.

Previdi, M., K. L. Smith, and L. M. Polvani, 2013: The Antarctic atmospheric energy budget. Part I: Climatology and intraseasonal-to-interannual variability. *J. Climate,* **26,** 6406–6418.

Randel, W. J., and F. Wu, 2007: A stratospheric ozone profile data set for 1979–2005: Variability, trends, and comparisons with

column ozone data. *J. Geophys. Res.,* **112,** D06313, doi:10.1029/2006JD007339.

Rossow, W. B., and R. A. Schiffer, 1999: Advances in understanding clouds from ISCCP. *Bull. Amer. Meteor. Soc.,* **80,** 2261–2287.

Sallée, J. B., K. G. Speer, and S. R. Rintoul, 2010: Zonally asymmetric response of the Southern Ocean mixed-layer depth to the southern annular mode. *Nat. Geosci.,* **3,** 273–279, doi:10.1038/ngeo812.

Serreze, M. C., A. P. Barrett, A. G. Slater, M. Steele, J. Zhang, and K. E. Trenberth, 2007: The large-scale energy budget of the Arctic. *J. Geophys. Res.,* **112,** D11122, doi:10.1029/2006JD008230.

Smith, K. L., L. M. Polvani, and D. R. Marsh, 2012: Mitigation of 21st century Antarctic sea ice loss by stratospheric ozone recovery. *Geophys. Res. Lett.,* **39,** L20701, doi:10.1029/2012GL053325.

Son, S.-W., N. F. Tandon, L. M. Polvani, and D. W. Waugh, 2009: Ozone hole and Southern Hemisphere climate change. *Geophys. Res. Lett.,* **36,** L15705, doi:10.1029/2009GL038671.

——, and Coauthors, 2010: Impact of stratospheric ozone on Southern Hemisphere circulation change: A multimodel assessment. *J. Geophys. Res.,* **115,** D00M07, doi:10.1029/2010JD014271.

Steig, E. J., D. P. Schneider, S. D. Rutherford, M. E. Mann, J. C. Comiso, and D. T. Shindell, 2009: Warming of the Antarctic ice-sheet surface since the 1957 International Geophysical Year. *Nature,* **457,** 459–462, doi:10.1038/nature07669; Corrigendum, **460,** 766.

Thompson, D. W. J., S. Solomon, P. J. Kushner, M. H. England, K. M. Grise, and D. J. Karoly, 2011: Signatures of the Antarctic ozone hole in Southern Hemisphere surface climate change. *Nat. Geosci.,* **4,** 741–749, doi:10.1038/ngeo1296.

Trenberth, K. E., 1991: Climate diagnostics from global analyses: Conservation of mass in ECMWF analyses. *J. Climate,* **4,** 707–722.

——, 1997: The definition of El Niño. *Bull. Amer. Meteor. Soc.,* **78,** 2771–2777.

——, and A. Solomon, 1994: The global heat balance: Heat transports in the atmosphere and ocean. *Climate Dyn.,* **10,** 107–134.

——, and J. T. Fasullo, 2010: Simulation of present-day and twenty-first-century energy budgets of the southern oceans. *J. Climate,* **23,** 440–454.

——, ——, and J. Kiehl, 2009: Earth's global energy budget. *Bull. Amer. Meteor. Soc.,* **90,** 311–323.

Turner, J., and S. Colwell, 2004: The SCAR READER project: Toward a high-quality database of mean Antarctic meteorological observations. *J. Climate,* **17,** 2890–2898.

Waugh, D. W., F. Primeau, T. Devries, and M. Holzer, 2013: Recent changes in the ventilation of the southern oceans. *Science,* **339,** 568–570, doi:10.1126/science.1225411.

WMO, 2010: Scientific assessment of ozone depletion: 2010. Global Ozone Research and Monitoring Project Rep. 52, 516 pp. [Available online at http://www.esrl.noaa.gov/csd/assessments/ozone/2010/report.html.]